IEEE Access
Multidisciplinary ⋮ Rapid Review ⋮ Open Access Journal

Received 23 November 2023, accepted 18 December 2023, date of publication 25 December 2023,
date of current version 3 January 2024.

Digital Object Identifier 10.1109/ACCESS.2023.3347197

APPLIED RESEARCH

Highly Integrated Low-Profile Multilayer Dual-Polarized Phased Array Antenna With Truncated Cavities for First Pulsed Bistatic L-Band Airborne SAR Sensor

DIEGO LORENTE[1], MARKUS LIMBACH[1], BERND GABLER[1], (Member, IEEE), HÉCTOR ESTEBAN[2], (Senior Member, IEEE), AND VICENTE E. BORIA[2], (Fellow, IEEE)

[1]SAR-Technology, Microwaves and Radar Institute, German Aerospace Center (DLR), 82234 Weßling, Germany
[2]Instituto de Telecomunicaciones y Aplicaciones Multimedia, Universitat Politècnica de València, 46022 Valencia, Spain

Corresponding author: Diego Lorente (diego.lorentecatalan@dlr.de)

ABSTRACT Synthetic Aperture Radar (SAR) has become, nowadays, one of the most important techniques in remote-sensing, and the increasing interest in Earth monitoring reinforces this trend. Next-generation SAR sensors will enhance the radar resolution capabilities by means of digital beamforming (DBF) techniques along with multistatic systems. In order to support the technological development of future spaceborne SAR missions, airborne sensors become an essential scope of research. Thereby, future airborne SAR systems demand enhanced DBF capabilities that involve phased array antennas with a high density of array elements. However, the antenna aperture size is significantly limited in airborne applications, which leads to low-profile and highly integrated antenna solutions, becoming a more challenging task for lower frequency operations such as L-band. In this work, a compact L-band dual-polarized multilayer phased array antenna with beam steering in elevation, developed for the next-generation German Aerospace Center (DLR) airborne SAR system, is presented. The proposed design makes use of truncated cavities to improve the array element isolation and provides 66% more antenna elements than the previous L-band phased array of the current DLR airborne SAR sensor with the same antenna aperture size. Measurements of a manufactured prototype show an antenna bandwidth of almost 20%, matching levels better than 17 dB, up to 15 dB gain, and cross-polarization suppression values higher than 35 dB. Thus, the proposed work will allow the application of advanced DBF techniques in the upcoming first pulsed bistatic L-band airborne SAR sensor.

INDEX TERMS Airborne, beamforming, bistatic, integration, phased array antenna, truncated cavity, synthetic aperture radar.

I. INTRODUCTION

Synthetic Aperture Radar (SAR) provides high-resolution imaging data on a global scale, with day-and-night and weather-independent operational capabilities. Due to its versatility and wide scope of applications, SAR has become one of the most well-established earth remote-sensing techniques in our time [1].

Making use of the penetrating properties of electromagnetic waves at lower frequencies, SAR allows for monitoring vegetation density or estimating forest height using tomography, as well as performing geological and glaciological studies with subsurface imaging, among other applications.

Precisely, the public concern about climate change and global warming has boosted the demand for spaceborne SAR sensors for environmental studies [2]. In addition, upcoming SAR satellite missions reaffirm this rising interest in Earth surface monitoring systems [3].

The associate editor coordinating the review of this manuscript and approving it for publication was Diego Masotti.

Next-generation SAR sensors will be driven by the demand to achieve higher resolution imaging along wider swaths. Thereby, future SAR systems will make use of advanced imaging modes by means of digital beamforming techniques along with bistatic and multistatic constellations [4], [5], [6].

In order to support the development of upcoming space-borne SAR systems, airborne sensors are employed. Due to their operational flexibility, they are used to test new radar concepts, novel signal processing methods, and state-of-the-art hardware [7], [8], [9]. Thus, airborne SAR sensors can be considered at the forefront of technological development.

Only a few bistatic airborne SAR sensors have been launched so far [10], [11], and to the best of the author's knowledge, only one L-band airborne bistatic SAR system employing two aircrafts has been implemented, but operating as a Frequency Modulated Continuous Wave (FMCW) radar [12]. The German Aerospace Center (DLR) is currently developing an advanced pulsed bistatic L-band airborne SAR sensor, that is meant to support the scientific development of the future Tandem-L satellite mission [3]. Thus, this new system will become the first pulsed bistatic L-band airborne SAR sensor.

Due to the side-looking operation of airborne SAR sensors, phased array antennas with beam steering capabilities are usually employed. SAR antennas are typically implemented in planar technology, due to their integration and miniaturization features [13], [14], [15], [16], [17]. In addition, planar antennas provide low-profile and reduced-cost solutions, that are extremely versatile for electrically controlled beamforming applications with high density of array elements.

The increasing complexity of future SAR systems also leads to more demanding requirements such as wider bandwidths to improve the range resolution [18], dual linear polarized antennas to apply polarimetric techniques [19], and highly integrated hardware to be installed on multistatic systems [20]. In addition, the key technology to enhance future SAR resolution capabilities is digital beamforming, which allows switching between different antenna looking angles in transmission and reception.

The beamforming capabilities of the system are strongly determined by the number of array elements. However, enhancing the radiation properties of the SAR antenna by maximizing the density of array elements is a demanding task for airborne applications, where the antenna aperture size is extremely limited on the aircraft structure. Thus, the efficient exploitation of the antenna aperture leads not only to an antenna miniaturization, which becomes even more challenging for lower frequency operations but also to a closer disposition of array elements. The latter approach inherently involves methods to mitigate the coupling effects among them.

Some well-known approaches to reduce the inter-element coupling in array antennas use electromagnetic bandgaps (EBGs) [21], [22]. However, multilayer antenna stacked structures make its implementation difficult. In addition, the repetition pattern of EBGs demands high inter-element spacings. Alternative solutions, such as defected ground structures (DGS) [23] are not suitable in aperture-coupled feeding antennas, due to the modification of the ground plane. A cost-effective non-planar approach is to place the antenna element within a closed casing structure or isolation walls such as a cavity box [24], [25]. This antenna assembly improves the antenna isolation along the E-plane. However, the influence of the electric walls and their proximity to the array elements also reduces the antenna bandwidth. Furthermore, since it is a closed structure, its mechanical realization for large planar arrays is extremely complex.

An alternative to those solutions is to separate the array elements using truncated cavities or casing structures with incompleted walls. Thus, the resonances are not as intense as the closed cavity since the structure is partially opened, which mitigates the bandwidth reduction, as well as the isolation between elements remains high. In addition, another advantage of using truncated cavities is that the isolation is more symmetric for both E- and H-planes.

In this work, a compact multilayer dual-polarized L-band phased array antenna of 40 elements for airborne SAR applications is designed, manufactured, and measured. The proposed solution makes use of solid truncated cavities to enhance the antenna element isolation, in order to achieve a high density of array elements by using a tight inter-element spacing of $0.48\lambda_0$. The presented phased array is built from two mirrored subarray antennas [26] and provides beam steering in elevation. In order to extend the degree of compactness, the feeding network is directly integrated within the antenna housing assembly, by which no electrical interconnection with cables is needed.

In addition, the proposed design provides 66% more array elements than the previous L-band antenna of the current operative DLR's airborne SAR sensor [7], considering the same antenna aperture size. Thereby, the enhanced radiation capabilities of the presented antenna will become the key feature to test advanced DBF techniques in the next-generation first L-band pulsed bistatic airborne SAR sensor.

This work is organized as follows: first of all, in section II, the SAR application is highlighted and the system requirements are explained. Later, in section III, the single antenna element based on a dual polarized aperture-coupled stacked patch antenna enclosed in a truncated cavity is introduced. Consequently, the design of a planar phased array of 5×8 elements, as well as its feeding network configuration and mechanical assembly are described in sections IV and V, respectively. Next, the measurements of a manufactured prototype are shown and discussed in section VI. Finally, the proposed antenna is compared with similar works in section VII, and it is fully validated in the last section VIII of this paper.

II. BISTATIC AIRBORNE SAR SYSTEM REQUIREMENTS

Bistatic airborne SAR sensors make use of the spatial separation between the transmitter and receiver to exploit

the different looking acquisition geometries, by which the resolution capabilities and the target detection and classification are improved. Thereby, the transmitter and receiver antennas can be installed on the same aircraft [10] or in multiple ones [11], [12], which provides different baselines for across-track and along-track interferometric applications using diverse aircrafts formations.

L-band SAR sensors are usually employed for forest monitoring, glaciology and subsurface imaging, due to the wave penetrating capabilities at larger wavelenghts.

In the framework of the DLR's DuoLIM project, an L-band pulsed polarimetric bistatic airborne SAR system is currently under development. Only one L-band bistatic airborne SAR sensor has been reported in literature [12], but operating as a FMCW radar. In comparison with pulsed radars, FMCW radar systems are limited in range resolution due to the lower transmitted power, which restraints its functional capabilities, such as flying altitude and imaged swath. Pulsed radars overcome these limitation at the cost of a higher complexity. Moreover, airborne hardware has to be certified to fulfill the airworthiness requirements.

For the new pulsed bistatic airborne SAR operation, a new dedicated flight-certified phased array antenna system, with beam steering in elevation, is required. The typical side-looking acquisition geometry in airborne SAR applications is depicted in Fig. 1.

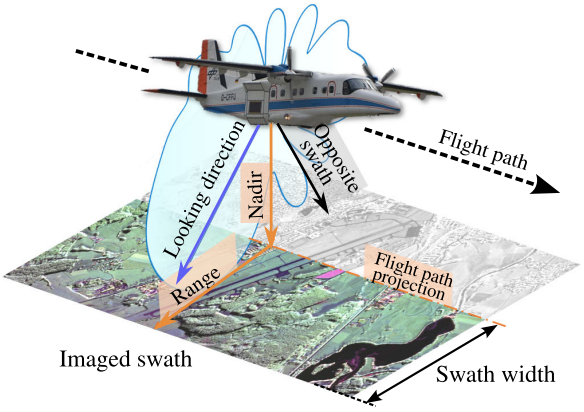

FIGURE 1. Side-looking SAR acquisition geometry.

The antenna will be installed beneath two aircrafts Dornier Do-228, in a circular holding platform or antenna carrier, as it is seen in Fig. 2. The antenna aperture size is 85.5 cm × 53 cm, and it is given by the limited available space on the antenna carrier. In addition, the installment position under the aircraft, along with the antenna carrier rotation platform, allows several swath illumination configurations under different looking angles, unlike other airborne SAR systems where the antenna is mounted sideways.

The system requirements are listed in Table 1. Additionaly, in airborne SAR applications, a higher suppression in nadir and opposite swath direction should be fulfilled, in order to mitigate the strong echoes coming from the perpendicular direction to the aircraft flight path, and to attenuate the contribution of the opposite imaged area, respectively.

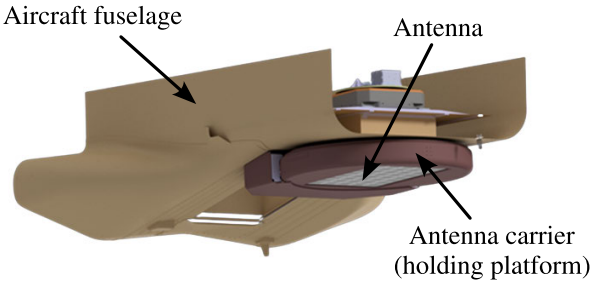

FIGURE 2. Antenna installment position under the aircraft.

TABLE 1. SAR system requirements.

Airborne SAR system requirements	
Frequency of operation	1.325 GHz
Bandwidth	150 MHz
Side-looking SAR acquisition	Beam steering in elevation at 42°
Half-Power Beamwidth	35°(Elevation) / 15°(Azimuth)
Polarimetric SAR	Dual-linear polarization
Side Lobe Level (SLL)	$\geq$ 18 dB
Cross-polarization suppression	$\geq$ 25 dB
Antenna aperture size	85.5 cm × 53 cm

III. DESIGN OF THE ANTENNA SINGLE ELEMENT

The array element is implemented in planar technology, due to its integration capabilities and adaptability for beamforming applications. The single element is based on a dual-polarized aperture coupled stacked patch antenna, which allows designing independently the radiation and feeding parts.

Due to the limited antenna aperture on the aircraft and the operational frequency in L-band, an additional miniaturization effort has to be applied in order to achieve a compact antenna implementation.

The antenna simulation and optimization have been performed with HFSS, a commercial software for full-wave electromagnetic (EM) analysis [27].

A. BANDWIDTH ENHANCEMENT

In order to improve the antenna bandwidth, a stacked patch configuration is implemented, with two microstrip patches spaced by low dielectric permittivity layers [28], [29]. The dual-polarization characteristic of the antenna leads to square patches, that resonate at slightly different frequencies due to their different geometries, thus increasing the antenna bandwidth. The top patch is placed below the upper substrate that serves as a superstrate, i.e radom layer, to protect it from atmospheric and aircraft conditions. The multilayer antenna assembly is depicted in Fig. 3 where the electrical properties of the different layers are listed in Table 2. The size of the single antenna element is 97.1 mm × 97.1 mm × 24.44 mm.

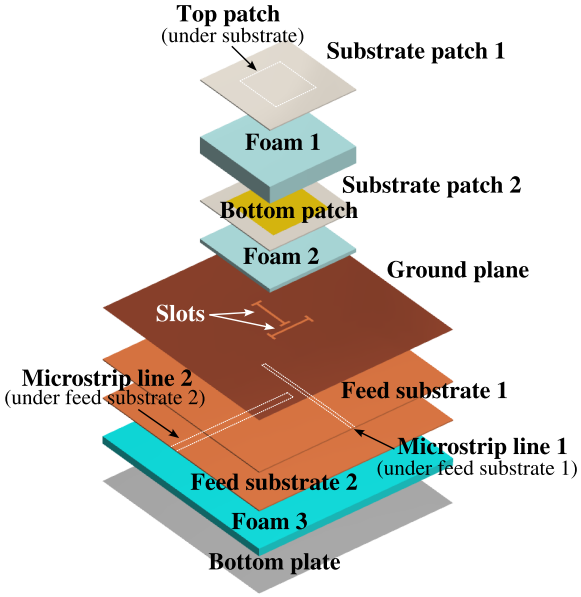

FIGURE 3. Antenna multilayer structure.

TABLE 2. Electrical properties of each antenna layer.

Layer	Substrate	ε_r	Thickness
Substrate patch 1	Rogers RO4360G2	6.15	1.22 mm
Foam 1	Rohacell HF51	1.06	18 mm
Substrate patch 2	Rogers RO4360G2	6.15	1.22 mm
Foam 2	Rohacell HF51	1.06	4 mm
Feed substrate 1	Rogers RO4360G2	6.15	1.22 mm
Feed substrate 2	Rogers RO4360G2	6.15	1.22 mm
Foam 3	Rohacell HF51	1.06	6 mm

B. APERTURE COUPLING FEEDING

The antenna is excited by means of an aperture slot that is etched on the ground plane, and is coupled by a 50-Ω microstrip line placed below. The aperture coupling feeding technique provides versatility to implement the dual-linear polarization property of the antenna, by which each polarization is excited with a different slot. The H-shaped aperture improves the coupling between the slot and the bottom patch [30]. The geometrical disposition of the slots, given by their offset, enhances the isolation between both polarizations. In addition, each feeding line is placed on a different substrate height to reduce the coupling between polarization feeding networks. As convention, the slots placed along x- and y-axis excite the horizontal and vertical polarization, respectively.

The geometrical parameters of the radiation part of the antenna (patches), and the feeding, namely coupling slots and microstrip lines, are depicted in Fig. 4 and listed in Table 3.

C. TRUNCATED CAVITY ASSEMBLY

The antenna aperture size is usually limited in airborne applications since the allocation space on the aircraft is restricted. Thus, in order to efficiently exploit the antenna aperture for next-generation SAR advanced beamforming

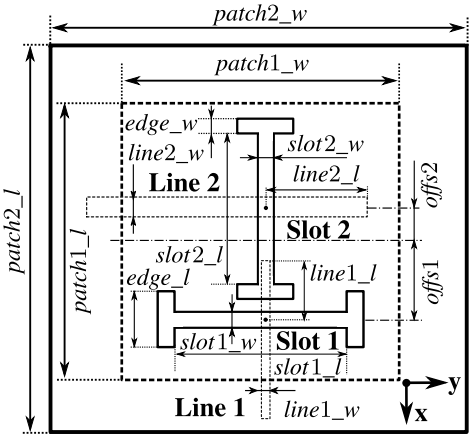

FIGURE 4. Patches and coupling slots layout.

TABLE 3. Patch size and feeding parameters (in mm).

Patch size		Aperture coupling feeding geometry					
patch1_l	58	*slot1_l*	38	*slot1_w*	2.5	*slot2_l*	37
patch1_2	59.4	*slot2_w*	2.5	*offs1*	17	*offs2*	8
patch2_l	63	*line1_l*	12.2	*line2_l*	19.7	*line1_w*	1.4
patch2_2	66	*line2_w*	3.7	*edge_l*	11	*edge_w*	2.5

applications, a closer disposition of array elements has to be considered. In the proposed work, an inter-element spacing of $0.48\lambda_0$ is used. Thereby, for the given antenna aperture on the aircraft, a phased array of 40 antenna elements (5×8) can be deployed, which greatly maximizes the density of array elements.

Reducing the spacing between array elements leads irreducibly to a higher inter-element coupling. Thus, in order to excite each antenna element independently, the coupling among them should be low enough. Some well-known planar techniques use EBGs structures to reduce the coupling between elements [21], [22]. However, the multilayer nature of the antenna, as well as the use of foam layers and the lack of space between array elements, prevent its application. Other approaches make use of cavities or closed assemblies to interrupt the propagation of surface waves and thus, enhance the antenna isolation [24], [25].

Nevertheless, due to the resonant nature of cavities, the antenna bandwidth is reduced, as well as the coupling is only improved in E-plane. In addition, the presence of soft low dielectric permittivity materials prevents the use of plated holes or vias, which forces a solid implementation of the electric walls. Precisely, this becomes a manufacturing disadvantage for large planar arrays applications, since the mechanical realization of corners is extremely complex.

In this work, the array element is enclosed in a truncated cavity assembly, composed of four aluminum solid walls of length $wall\_l = 86.1$ mm, thickness $wall\_th = 11.5$ mm, and height $wall\_h = 24.44$ mm, as shown in Fig. 5. The antenna ground plane is made of aluminum with a thickness of 1.2 mm. The four solid walls are attached on the ground plane using countersunk screws.

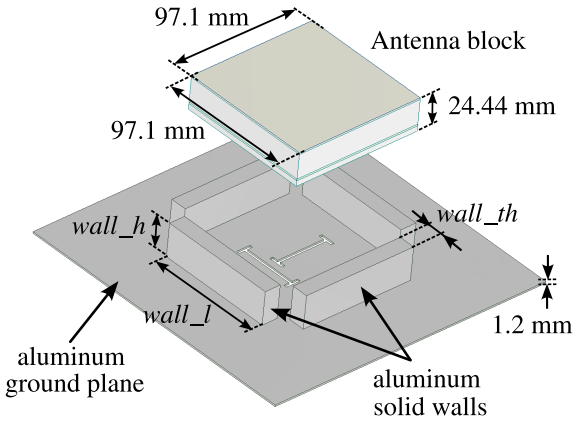

FIGURE 5. Antenna element truncated aluminum assembly.

A comparison in terms of coupling S_{21} between two single-polarized aperture-coupled stacked patch antennas spaced $0.48\lambda_0$ is shown in Fig. 6. In this analysis, the same electrical antenna is considered in three different configurations: in free space, i.e without isolation improvement, inserted in a closed cavity box, and within the proposed truncated assembly. It can be noted that, for the center frequency of operation 1.325 GHz, both closed cavity and the truncated assembly improve the coupling in E-Plane with isolation values up to 17 dB. However, while using the closed cavity the coupling in H-Plane increases, in the case of the truncated assembly the values remain comparable.

Thus, with the proposed truncated cavity, symmetric isolation levels in both antenna planes of approximately 17 dB can be achieved, which are reasonable considering the close proximity between antenna elements. In addition, the mitigation of the antenna bandwidth (when using closed cavities) is reduced, since the structure is not completely closed.

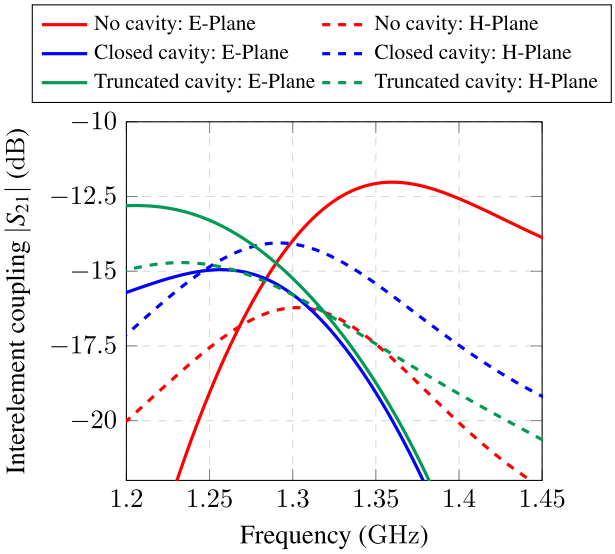

FIGURE 6. Analysis of the coupling S_{21} between two single-polarized antenna elements, considering an inter-element spacing of $0.48\lambda_0$ and three different isolation configurations.

Furthermore, since there are no corners involved in the realization of the antenna casing, the mechanical construction of the proposed solution for planar arrays with a high density of elements is considerably simplified.

Thus, and despite its mechanical simplicity, the proposed truncated cavity assembly becomes a low-profile, compact and cost-effective non-planar isolation method, that arises as a convenient alternative when other planar solutions are not feasible to be implemented.

An additional copper layer of thickness 35 μm, that serves as a feeding network ground plane, is placed below the aluminum ground plane. This assembly demands an accurate alignment of these two layers, since the coupling slots are etched on both ground planes. The feeding network is fixed below the antenna ground plane with screws, to assure the electrical continuity between aluminum and copper layers.

D. MEASUREMENT OF A MANUFACTURED SINGLE ELEMENT PROTOTYPE

The measured S-parameters of a manufactured single antenna element is depicted in Fig. 7.

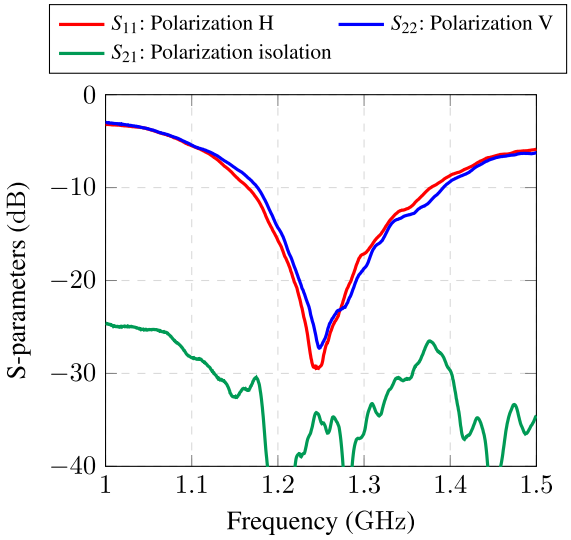

FIGURE 7. Measured S-parameters single antenna element prototype.

The measured prototype achieves a comparable return loss for both polarizations with an operational bandwidth higher than 200 MHz, that leads to relative bandwidth of approximately 18%, measured at −10 dB. Despite that the antenna performance is slightly shifted towards lower frequencies, certainly due to fabrication and construction tolerances, the antenna matching level at the center frequency of operation remains better than 15 dB.

The measured polarization isolation $|S_{21}|$ is mainly lower than 30 dB in the entire operational bandwidth. The antenna gain is 5.2 dB and 5.4 dB for the horizontal and vertical polarization, respectively.

IV. DESIGN OF A PLANAR PHASED ARRAY OF 5 × 8 ELEMENTS

In order to exploit the antenna aperture on the aircraft, and to maximize the number of array elements for beamforming applications, a tight inter-element spacing of $0.48\lambda_0$ is used. Thus, for the given antenna aperture size, a phased array of 5×8 elements can be arranged.

The array topology is shown in Fig. 8, and it is composed of two mirrored subarrays of 5×4 elements. The feeding configuration is split in two levels: azimuth and elevation.

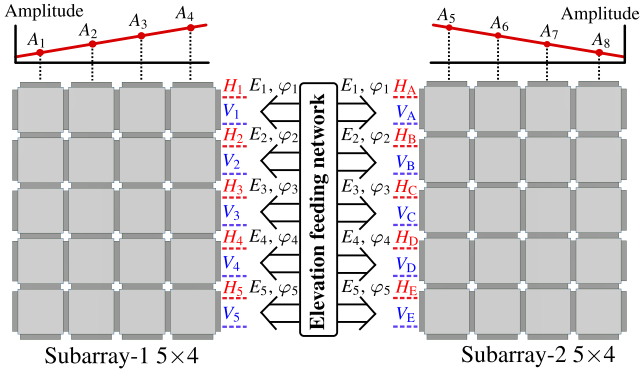

FIGURE 8. Array feeding configuration.

The azimuth feeding network excites the antenna elements of each array row in phase with the proper amplitude distribution, being $H_{1\text{-}5}$, $H_{\text{A-E}}$, $V_{1\text{-}5}$, $V_{\text{A-E}}$ the feeding inputs for each polarization and array row. Due to the antenna symmetry, the azimuth network is composed of two electrical identical mirrored feeding networks, each of one excites a subarray 5×4 [26].

The elevation network is an additional feeding topology, that provides the beamforming in elevation by applying a progressive phase difference $\varphi_{1\text{-}5}$ and an amplitude distribution $E_{1\text{-}5}$.

The resulting array factor can be expressed as:

$$\begin{aligned} FA(\theta,\phi) &= FA(\theta,\phi)_{El} \cdot FA(\theta,\phi)_{Az} \\ &= \sum_{m=0}^{3} E_{\text{m+1}} \cdot e^{(jm\frac{0.48}{\lambda_0} sin\theta cos\phi + \varphi_{\text{m+1}})} \\ &\quad \cdot \sum_{n=0}^{7} A_{\text{n+1}} \cdot e^{(jn\frac{0.48}{\lambda_0} sin\theta sin\phi)} \end{aligned}$$

where, due to the antenna symmetry:

$$A_{\text{n+5}} = A_{\text{4-n}}\,, n \in [0, 3]$$

A. AZIMUTH FEEDING NETWORK

The azimuth network excites each of the five array rows, feeding each antenna element in phase and providing a triangular amplitude tapering in order to reduce the side lobe level, thus mitigating possible radar ambiguities in azimuth direction.

The feeding topology in azimuth is implemented by means of two identical electrical mirrored multilayer feeding networks, that excite each subarray providing an amplitude distribution given by a ramp-type function. Thus, when considering the entire array, a triangular amplitude tapering is achieved along azimuth direction, as it is seen in Fig. 8. In addition, splitting the feeding network in two halves also eases its fabrication, since the electrical size of the feeding network for the entire array prevents its manufacturing.

Each polarization feeding network is implemented in microstrip technology and placed on different substrate positions, as depicted in Fig. 3, in order to enhance the isolation between networks. In addition, also the substrate Rogers RO4360G2 is used ($\varepsilon_r = 6.15, \tan\delta = 0.0038$) due to its high dielectric permittivity, in order to reduce the electrical size of the feeding network.

The ramp amplitude distribution of each feeding row is achieved by means of a combination of balanced and unbalanced power dividers along with 10 dB-coupler lines, as it is seen in Fig. 9. The layout of each polarization feeding network has been optimized in order to avoid the intersection of microstrip lines from different polarization networks that could reduce the polarization isolaton. Furthermore, the electrical length of the feeding path that excites each coupling slot is comparable, in order to achieve a similar feeding phase variation in frequency for each antenna element.

The resistors of the Wilkinson power dividers are implemented using thin resistive films, a technology by which the use of lumped resistors are replaced by resistive foils [31]. Thereby, the soldering of discrete elements is avoided and a more homogeneous performance can be achieved, which becomes extremely advantageous for multilayer applications. The excitation of each feeding input is performed with SMP connectors, since they provide a given radial and misalignment tolerance that make them robust against vibration effects that can occur during the flight [32].

The power distribution for each antenna element and polarization is listed in Table 4. It can be noted that the amplitude distribution for both polarizations $A_1 - A_4$ slightly differs. The reason for that is the limited available space that influences the layout design for both polarization feeding networks. Thereby, the feeding network of the vertical polarization, due to its electrical size, is based on two power dividers along with a 10-dB coupler line, unlike the horizontal polarization, where three different power dividers are combined.

TABLE 4. Amplitude distribution in azimuth.

Horizontal polarization		Vertical polarization	
A_1	-10.9 dB	A_1	-14.9 dB
A_2	-8.7 dB	A_2	-9.5 dB
A_3	-6.6 dB	A_3	-5.7 dB
A_4	-3.6 dB	A_4	-3.8 dB

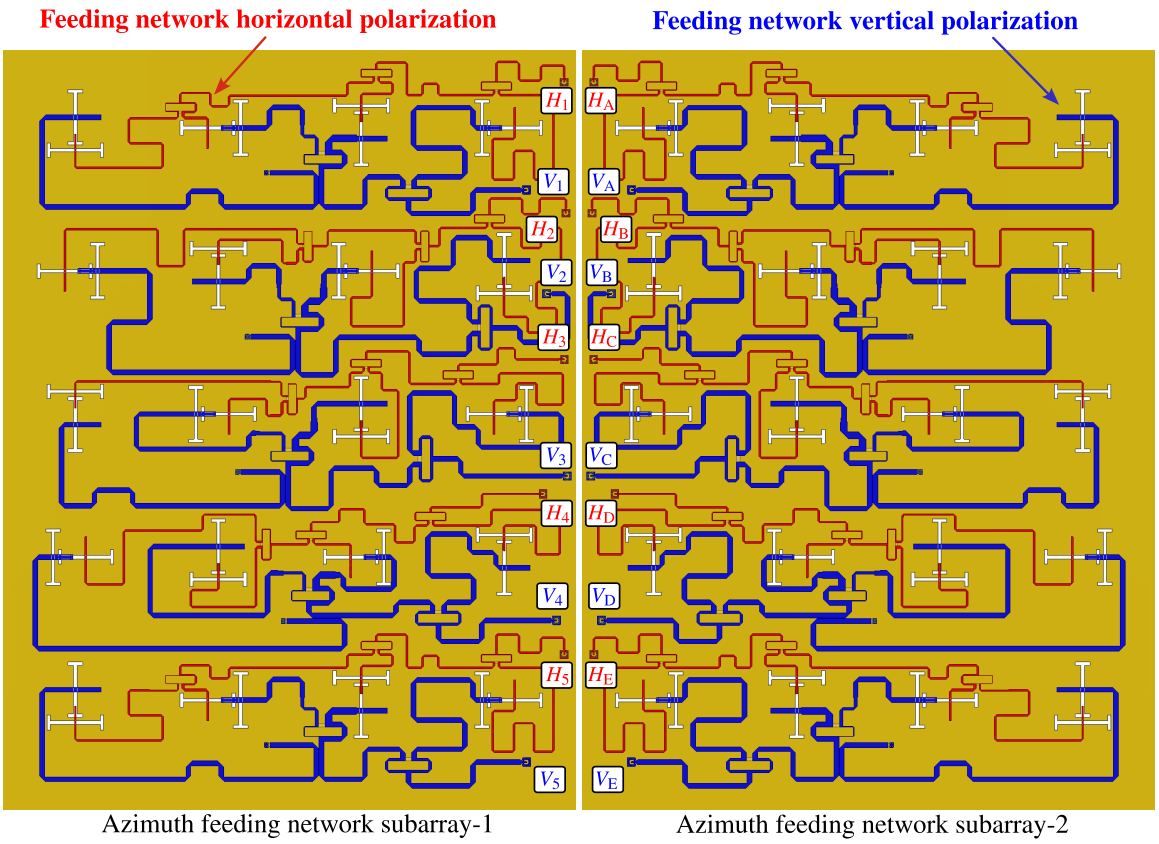

FIGURE 9. Azimuth feeding network. Each polarization feeding network lays on a different substrate height. For depiction purposes both networks are shown on the same level.

1) CROSS-POLARIZATION SUPPRESSION ENHANCEMENT

In order to improve the cross-polarization performance of the antenna, a sequential 90° rotation of the antenna elements in both array axis is applied [25], by which cross-polarization suppression values above 50 dB can be achieved. This rotation approach changes the slot position for each antenna element, alternating the slot offsets along the array axis, as it is seen in Fig. 9. Thus, this cross-polarization suppression method leads to a feeding topology where antenna elements with different slot feeding geometries are involved for the same polarization excitation.

It is known that shifting the slot position along E-plane produces a pattern tilt [33], slightly deviating the maximum of the radiation pattern from boresight direction. Thus, the phase of the radiated fields of an array element fed with a centered slot is not exactly the same as the equivalent antenna element excited by a shifted slot. Thereby, for a constructive interference of the radiated fields from array elements that are fed with different slot positions, a slight feeding phase variation has to be applied to those antenna elements that are excited with a slot offset. This effect is considered and compensated in the azimuth feeding network, so all the array elements are properly excited in phase.

B. ELEVATION FEEDING NETWORK

Despite the suitability of the proposed antenna for beamforming operations, the current application only demands a fixed beam steering. Thereby, the elevation feeding network provides the required beam steering at $\theta = 42°$ in elevation direction, in order to fulfill the side looking operation of SAR systems. Additional triangular amplitude weighting, in order to reduce the side lobe level in elevation, is also applied.

Each azimuth feeding row is excited by a progressive phase difference $\Delta\varphi$ to achieve the beam steering in the desired direction. This phase variation is given by:

$$\Delta\varphi = \frac{2\pi}{\lambda_0} d \sin\theta$$

which for the required elevation angle and the given inter-element spacing $d = 0.48\lambda_0$, it yields a progressive phase variation $\Delta\varphi \approx 115°$

The elevation feeding network is based on two independent polarization networks that excite all azimuth feeding rows for each subarray and polarization, as it is seen in Fig. 10. Due to space constraints, the power splitting to feed each subarray (1-5, A-E) is also realized on this network level.

Each polarization elevation network is designed in microstrip technology on the same substrate Rogers RO 4360G2 ($\varepsilon_r = 6.15$, $\tan\delta = 0.0038$) with thickness 1.22 mm.

The power distribution is based on different balanced power dividers, combiners and 10 dB couplers. A 180° phase difference has to be applied between the ports of each subarray for the vertical polarization $V_{1\text{-}5} - V_{\text{A-E}}$. This is due to the mirrored symmetry of the array, since the slots that excite the vertical polarization of each subarray are fed out of phase, i.e. the microstrip lines that couples one slot and its corresponding mirrored slot come from opposite directions.

Each polarization feeding network is excited with a connector type N model 864L1, due to its increased power handling in comparison with standard SMA connectors. SMP are used as output connectors since the interconnection between the elevation and azimuth network is performed by means of adjustable SMP bullet adapters.

The amplitude E_x and feeding phase φ_x for each azimuth feeding row, subarray and polarization is listed in Table 5. It can be noted that the phase difference between array elements $\Delta\varphi = |\varphi_{x+1} - \varphi_x|$ slightly differ from the theoretical value, since the radiation pattern has been simulated and later optimized to fulfill the system requirements.

TABLE 5. Amplitude distribution and phase variation in elevation.

Horizontal polarization			Vertical polarization		
H_1	E_1	φ_1	V_1	E_1	φ_1
	-17.27 dB	-124.17°		-17.24 dB	-101.93°
H_A	E_1	φ_1	V_A	E_1	φ_1
	-17.24 dB	-124.11°		-17.34 dB	-78.6°
H_2	E_2	φ_2	V_2	E_2	φ_1
	-10.07 dB	15.88°		-10.04 dB	2.79°
H_B	E_2	φ_2	V_B	E_2	φ_1
	-10.04 dB	15.94°		-10.15 dB	-176.94°
H_3	E_3	φ_3	V_3	E_3	φ_1
	-7.04 dB	135.7°		-6.98 dB	118.45°
H_C	E_3	φ_3	V_C	E_3	φ_1
	-7.01 dB	135.66°		-7.11	-61.27°
H_4	E_4	φ_4	V_4	E_4	φ_4
	-10.1 dB	-99.23°		-10.07 dB	-106.44°
H_D	E_4	φ_4	V_D	E_4	φ_4
	-10.07 dB	-99.22°		-10.19 dB	72.82°
H_5	E_5	φ_5	V_5	E_5	φ_5
	-17.21 dB	20.88°		-17.17 dB	2.73°
H_E	E_5	φ_5	V_E	E_5	φ_5
	-17.18 dB	20.93°		-17.26 dB	-176.83°

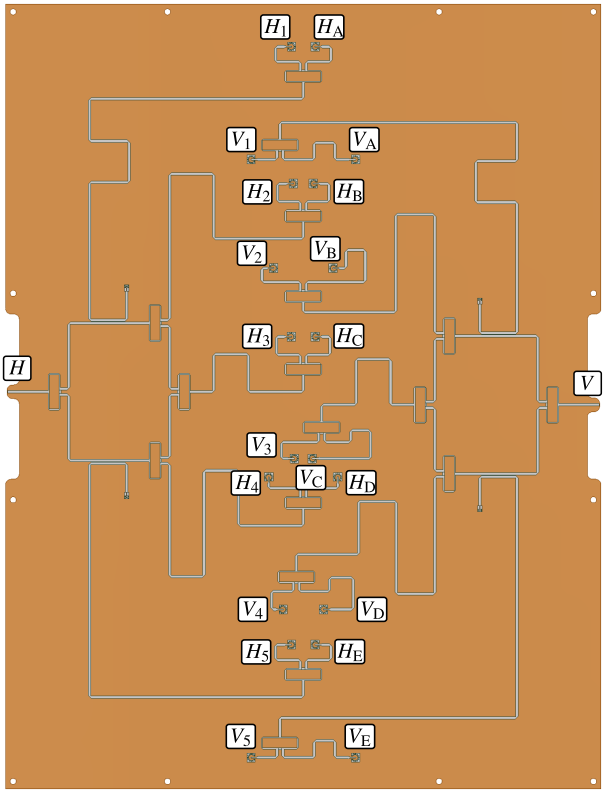

FIGURE 10. Elevation feeding network.

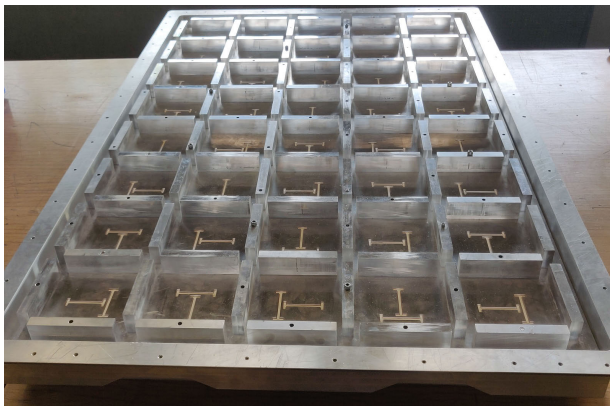

FIGURE 11. Antenna housing without array elements.

V. ANTENNA MECHANICAL ASSEMBLY

The radiation and feeding parts of the antenna are integrated within the same antenna housing that is made of aluminum, as it is seen in Fig. 11.

The whole structure is attached vertically by means of screws, whose position is set to fulfill the airworthiness requirements. The antenna elements are inserted within the truncated cavities. An additional grid cover is used for the mechanical stability of the array elements.

The azimuth and elevation feeding networks are interconnected by means of adjustable SMP adapters. This adjustability is achieved by means of a spring mechanism, by which the SMP adapter length can be modified. Thereby, the SMP output connectors of the elevation network that are placed on the same position, can be connected with the SMP input connectors of the azimuth network that are placed at different substrate heights. The SMP adapters go through the antenna casing, where the elevation network is attached to a cover plate and screwed to the back side of the antenna housing.

It can be noted that the interconnection between feeding network demands an extremely accurate alignment of the top and bottom SMP connectors, and the adaptors adjustment can only be achieved within a narrow aperture, as depicted in Fig. 12. Thereby, no internal cables are required, thus achieving a higher degree of integration.

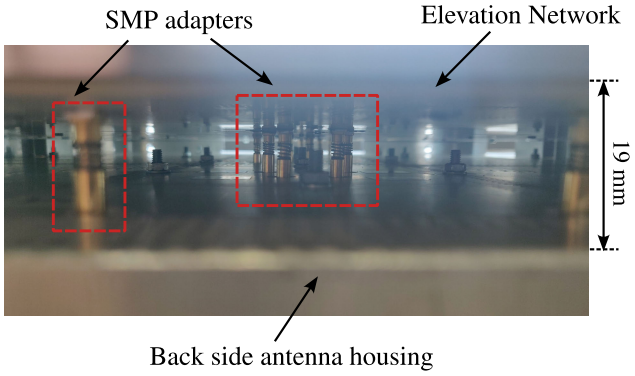

FIGURE 12. View of the connection between the azimuth and elevation feeding networks using adjustable SMP adapters.

The gap between the back side of the antenna casing and the azimuth feeding network is filled with a foam layer, in order to avoid air condensation that can occur at high aircraft altitudes. In addition, all RF conductor surfaces are provided with chemical Ni/Au coating to protect them from oxidation.

The complete mechanical assembly is depicted in Fig. 13

VI. MEASUREMENTS OF MANUFACTURED ANTENNA PROTOTYPE

The 40 array elements, along with the feeding networks and the antenna housing, have been manufactured, assembled and measured. Since the antenna has been constructed in different steps, the electrical performance of each integration phase has been previously tested.

A. MEASUREMENT OF THE ELEVATION NETWORK

The S-parameters of the elevation feeding network have been measured with the network analyzer model ZVA 24 of Rohde&Schwarz. The measured return loss levels show matching values better than 20 dB for the frequency band of operation, 1.25 GHz-1.4 GHz, which also leads to a good agreement with the simulated data.

The measured amplitude at each output for both polarization feeding networks and the corresponding simulated value are listed in Table 6.

As it can be seen, the difference between simulation and measurement is around 0.9 dB for the center output ports (H_3, H_C and V_3, V_C), while for the outer ports this variation is slightly higher than 1 dB. This is produced by the substrate losses, since this attenuation difference is dependent on the electrical path length between the input and the output ports. Even though the simulation values are calculated considering substrate losses, there is for sure a slight discrepancy between the value for the dielectric losses $\tan\delta$ given by the manufacturer and the real value. In addition, the measured values also include the insertion loss contributions of the connectors, power splitters, as well as conductor and ohmic losses. Furthermore, the insertion losses of the SMA-SMP adapters are also included in the measurement, since they are not considered in the calibration process.

Nevertheless, the measured phase and amplitude values, as well as the return loss and the port isolation, agree closely with the simulated data.

TABLE 6. Simulated and measured amplitude distribution of the elevation feeding network.

Horizontal polarization			Vertical polarization		
H_1	Simulation	-17.27 dB	V_1	Simulation	-17.24 dB
	Measurement	-18.5 dB		Measurement	-18.5 dB
H_A	Simulation	-17.24 dB	V_A	Simulation	-17.34 dB
	Measurement	-18.5 dB		Measurement	-18.6 dB
H_2	Simulation	-10.07 dB	V_2	Simulation	-10.04 dB
	Measurement	-11 dB		Measurement	-10.9 dB
H_B	Simulation	-10.04 dB	V_B	Simulation	-10.15 dB
	Measurement	-11 dB		Measurement	-11.1 dB
H_3	Simulation	-7.04 dB	V_3	Simulation	-6.98 dB
	Measurement	-7.95 dB		Measurement	-7.8 dB
H_C	Simulation	-7.01 dB	V_C	Simulation	-7.11 dB
	Measurement	-7.95 dB		Measurement	-8 dB
H_4	Simulation	-10.1 dB	V_4	Simulation	-10.07 dB
	Measurement	-11.07 dB		Measurement	-10.8 dB
H_D	Simulation	-10.07 dB	V_D	Simulation	-10.19 dB
	Measurement	-11.08 dB		Measurement	-11 dB
H_5	Simulation	-17.21 dB	V_5	Simulation	-17.17 dB
	Measurement	-18.5 dB		Measurement	-18.4 dB
H_E	Simulation	-17.18 dB	V_E	Simulation	-17.26 dB
	Measurement	-18.49 dB		Measurement	-18.5 dB

B. MEASUREMENT OF THE ANTENNA WITH INTEGRATED AZIMUTH FEEDING NETWORK

In this construction phase, the antenna is assembled and only the integration of the elevation network is missing. Thus, the S-parameters of each subarray antenna at different azimuth feeding rows and polarizations $H_{1\text{-}5}$, $H_{\text{A-C}}$, $V_{1\text{-}5}$, $V_{\text{A-C}}$ can been measured.

The measurement is performed through the back side of the antenna housing by means of bores through which the SMP adaptors go through, that allow to access each azimuth feeding port. A picture of the installment process of the azimuth feeding network is shown in Fig. 15.

The correspondence between the array row, polarization and subarray with the S-parameter subscript can be extracted from Fig. 9. Due to all possible S-parameters combinations, a few examples of the measured return loss, coupling levels and polarization isolation values are presented.

Fig. 16 shows measured return loss levels $S(H_x, H_x)$, $S(V_x, V_x)$ at different array rows for both polarizations. Measurements show matching levels mainly better than 10 dB for the operational bandwidth, with values beyond 20 dB at the center frequency of operation. In addition, it can be noted that the matching level of the same feeding row and polarization for different subarrays is quite comparable, since they are electrical identical.

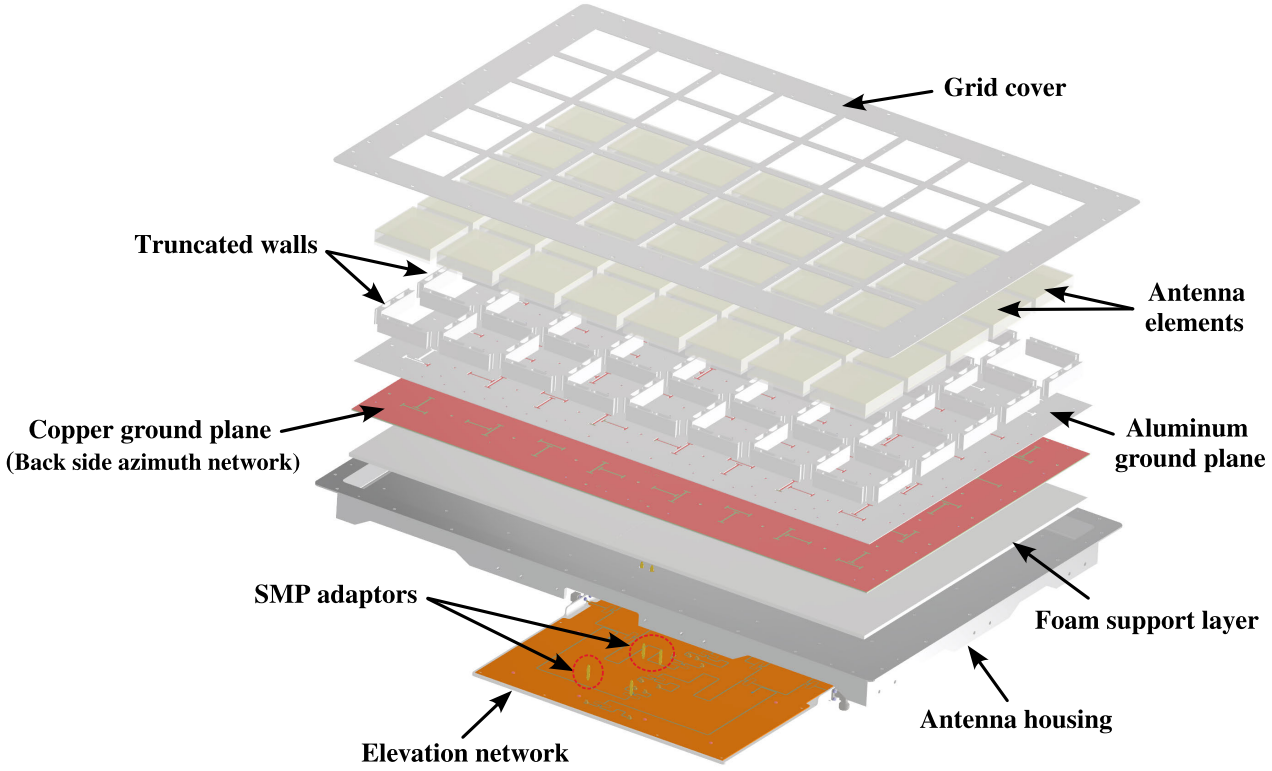

FIGURE 13. Antenna mechanical assembly.

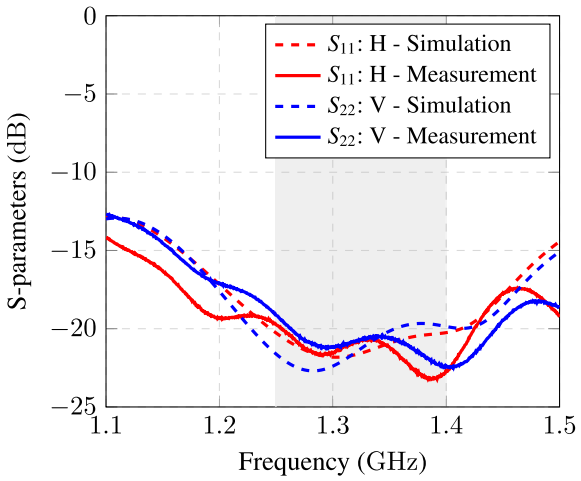

FIGURE 14. Comparison of simulated and measured S-parameters of the elevation network.

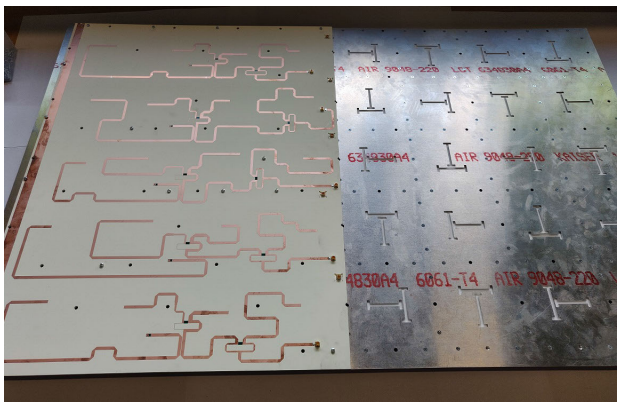

FIGURE 15. Integration azimuth feeding network. Bottom view.

The coupling levels $S(H_{x+1}, H_x)$, $S(V_{x+1}, V_x)$ between two closely located polarization feeding rows are shown in Fig. 17. Despite the close proximity of array elements, the isolation values mainly vary from 16 dB up to better than 20 dB, for the lowest and highest frquency bands of operation.

The polarization isolation levels $S(H_x, V_x)$ are depicted in Fig. 18. As it can be noted, the coupling between different polarization feeding rows is mainly better than −20 dB for the operational bandwidth, and lower than −25 dB for the center frequency of operation.

C. MEASUREMENT OF THE FINAL ANTENNA

The final assembled antenna is measured in the dual reflector Compact Antenna Test Range (CATR) at the Microwaves and Radar Institute of the German Aerospace Center [34].

The measured return loss is depicted in Fig. 19 and it shows a matching level higher than 15 dB for the entire operational bandwidth, as well as values better than 20 dB at the center frequency. Furthermore, the polarization isolation is far better than 25 dB for the frequency range of operation.

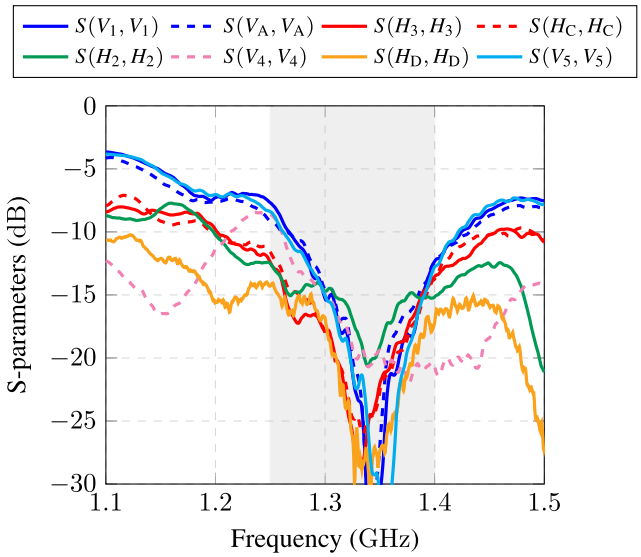

FIGURE 16. Measured return loss level at the azimuth feeding network.

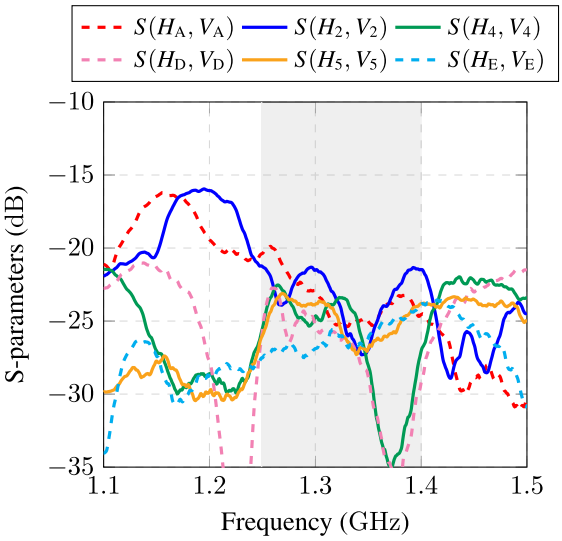

FIGURE 18. Measured polarization isolation levels at the azimuth feeding network.

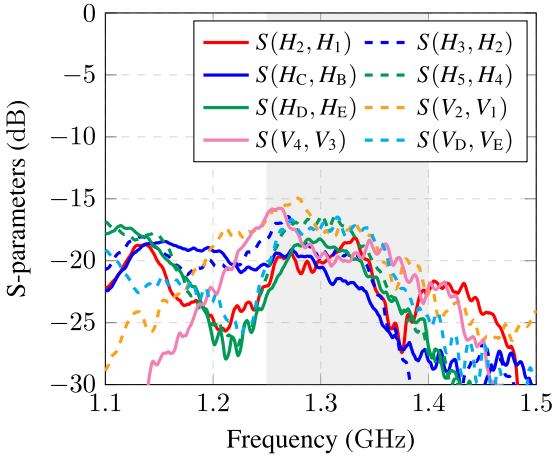

FIGURE 17. Measured coupling levels at the azimuth feeding network.

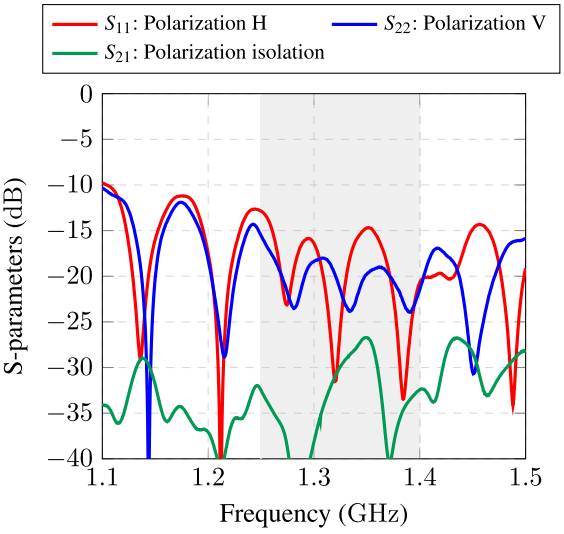

FIGURE 19. Measured S-parameters of the final assembled antenna.

A comparison between simulation and measurement of the normalized radiation pattern, in elevation and azimuth for the center frequency of operation 1.325 GHz, are shown in Fig. 20 and Fig. 21 respectively.

The measurements show excellent agreement with the simulations. The measured cross-polarization levels are higher than the simulated data, since the sensitivity required to measure cross-polarization suppression values around 50 dB is difficult to achieve. However, measured antenna cross-polarization suppression levels are still better than 35 dB, which is 10 dB beyond the system specifications. The side lobe level in both antenna planes is better than 20 dB with a slight asymetry in azimuth for the horizontal polarization, certainly due to fabrication or construction tolerances.

The measured antenna gain values are 14.2 dB and 15.1 dB for the horizontal and vertical polarization, respectively. This differs around 0.6 dB from the simulated data when considering the measured elevation amplitude weighting listed in Table 6. This gain variation is mainly due to the insertion losses of the connectors and the adjustable SMA-SMP adapters, as well as fabrication, assembly and possible measurement setup inaccuracies. In addition, the aforementioned insertion losses caused due to the substrate of the elevation network also leads to a unavoidable power loss due to the electrical size of the feeding layout. Nevertheless, the overall antenna performance agree really good with the simulation results and fulfills by far the system specifications.

A further analysis is performed in Fig. 22, where the beam steering stability within the operational bandwidth for both polarizations is shown. It can be noted that the measured cross-polarization suppression levels are far better than 30 dB with values beyond 40 dB.

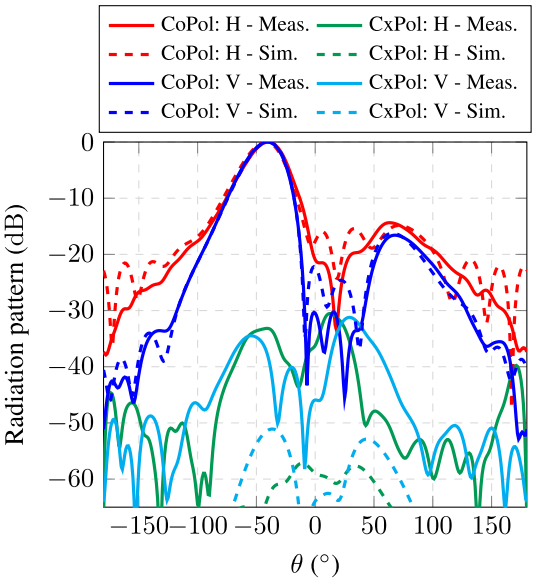

FIGURE 20. Measured normalized radiation pattern in elevation at 1.325 GHz for both polarizations.

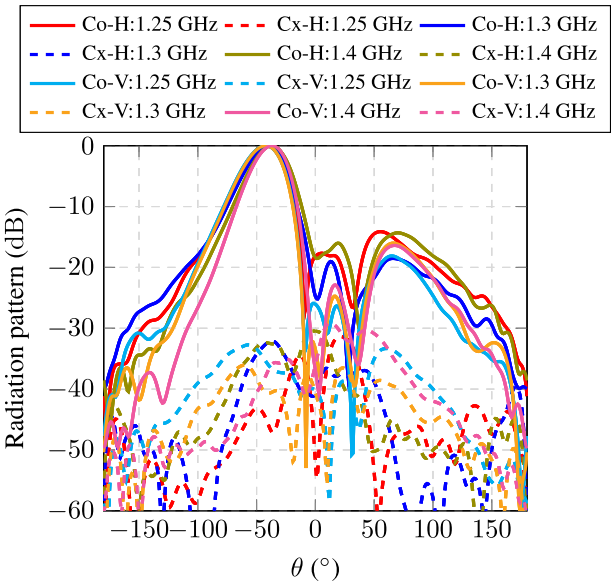

FIGURE 22. Measured normalized radiation pattern in elevation for 1.25 GHz, 1.3 GHz and 1.4 GHz.

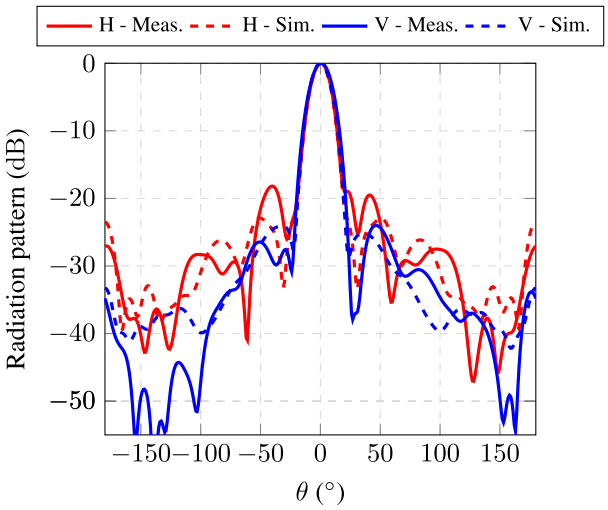

FIGURE 21. Measured normalized radiation pattern in azimuth at 1.325 GHz for both polarizations.

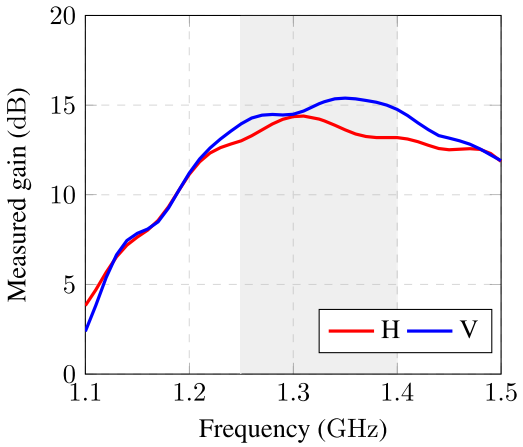

FIGURE 23. Measured gain over frequency for both polarizations.

Finally, the gain variation over frequency is depicted in Fig. 23. It can be seen that the maximum gain is slightly shifted in frequency for both polarizations, and a steady gain is achieved along the frequency range of operation.

VII. COMPARISON WITH OTHER WORKS

It can be noted that the enhanced element isolation due to the truncated cavities allows exciting more precisely each array element with the required amplitude and phase values. This way, the high density of array elements can be exploited to improve the beamforming capabilities, thus shaping more accurately the radiation pattern.

In order to get an overview of the level of compaction achieved with the proposed work, a comparison with other L-band SAR antennas is shown in Table 7. It can be noted the degree of integration obtained with the presented design, which even though a considerable miniaturization has been achieved, an antenna bandwidth of almost 20% is reached.

A further comparison can be performed with the current L-band antenna of the DLR's operative monostatic multi-frequency airborne SAR sensor, F-SAR [7]. Since the next-generation bistatic airborne SAR sensor and the actual F-SAR system are mounted on the same aircraft, the available antenna aperture size for both L-band antennas is the same.

Fig. 24 shows a comparison in terms of array elements between the current L-band array antenna (4×6 elements) and the proposed antenna (5×8 elements). It can be seen that the presented solution provides 16 more array elements, which leads to an improvement of 66% in the exact same

TABLE 7. Comparison of the proposed work with other L-band planar antennas for SAR applications.

Reference	Array elements	Size (λ_0^2)	Interelement spacing	Density array (Elements/Size)	Polarization	Relative bandwidth	Antenna type
[7]	4×6	2.34×3.77	$0.66\lambda_0 \times 0.44\lambda_0$	2.77	Dual linear	12%	Stacked patch
[13]	2×6	1.37×3.43	$0.55\lambda_0$	2.55	Dual circular	6.1%	Truncated square patch
[14]	2×6	1.59×4.57	$0.75\lambda_0$	1.65	Dual linear	35%	Single patch
[15]	2×2	1.38×1.46	$0.7\lambda_0$	1.98	Single linear	6.5%	Perforated patch
[16]	4×3	2.08×1.54	$0.53\lambda_0$	3.74	Dual linear	8%	Crossed slot
[17]	8×8	5.6×5.6	$0.7\lambda_0$	2.04	Dual linear	8%	Stacked perforated patch
This work	**5×8**	**2.34×3.77**	**$0.48\lambda_0$**	**4.53**	**Dual linear**	**18%**	**Stacked patch**

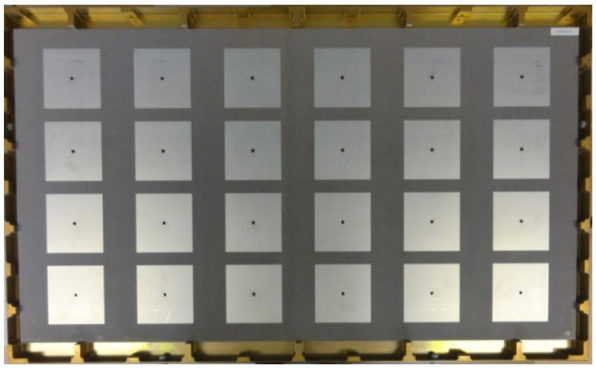

(a)

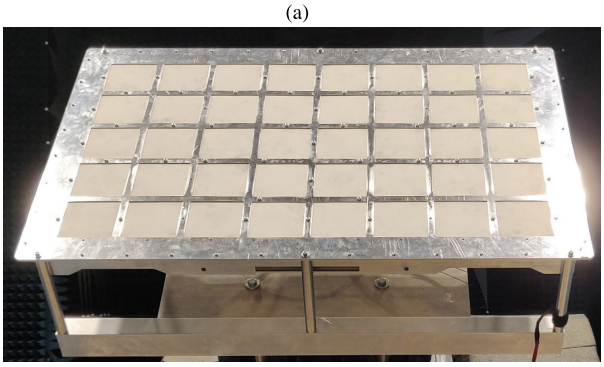

(b)

FIGURE 24. Comparison of the DLR SAR airborne L-band antennas with the same aperture size (a) Current antenna installed on F-SAR system (b) New L-Band antenna for DLR's next generation airborne SAR sensors.

TABLE 8. Comparison of the proposed design with the current operative DLR L-band antenna.

L-band antenna	Array elements	BW	Measured gain	
			Horizontal	Vertical
Current F-SAR	4×6	150 MHz	12.3 dB	13.8 dB
Proposed design	5×8	210 MHz	14.2 dB	15.1 dB
Improvement	16 (66%)	60 MHz	1.9 dB	1.3 dB

antenna aperture size. In addition, considering that both antennas are excited with a triangular amplitude distribution, the new solution also provides more antenna gain, due to the improved element isolation, as it is shown in Table 8. Futhermore, this gain increase should be also considered twice in the system performance, since due to the two way operation of SAR systems, the same antenna is used for both transmission and reception. The final assembled antenna can be seen in Fig. 25.

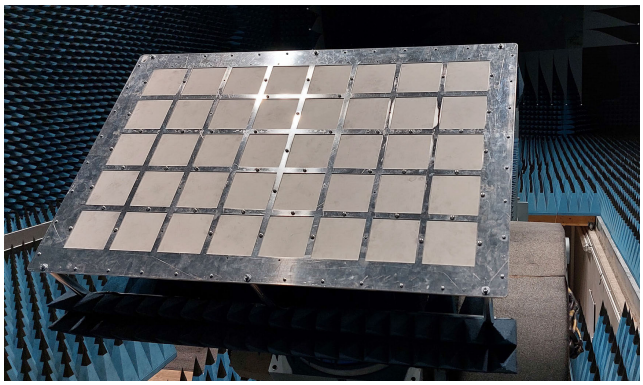

FIGURE 25. Final assembled antenna in the DLR's compact test range.

Thus, the proposed L-band phased array antenna will not only be implemented in the new bistatic DLR's airborne SAR sensor but also in the next-generation F-SAR system, with electrical beam steering switching capabilities.

VIII. CONCLUSION

This work presents a highly integrated low-profile multilayer dual-polarized phased array antenna for the first pulsed bistatic L-band airborne SAR sensor. The proposed design exploits efficiently the limited aperture size on the aircraft, by reducing the array inter-element spacing, and enhances the antenna element isolation using truncated cavities. Thus, the density of array elements can be maximized in order to enhance the beamforming capabilities required for next-generation SAR systems. In addition, the presented phased array is assembled in a flight-certified antenna housing, that allows the integration of the feeding network, thus achieving a higher degree of compactness required for airborne applications. The proposed solution is validated by means of a manufactured prototype that is constructed, assembled, and measured. Measurements show a good agreement with the simulation and despite the antenna compaction, a bandwidth of almost 20% is still achieved. Unavoidable internal feeding network substrate losses reduce the antenna gain, but good frequency stability of the beam steering and reduced side lobe level are achieved, as well as cross-polarization suppression values of 35 dB.

The presented phased array will also replace the L-band antenna of the current operative monostatic DLR's F-SAR system since the proposed design provides 66% more antenna elements for the same antenna aperture size, by which the shaping capabilities of the radiation pattern will be enhanced. Thus, the proposed antenna solution paves the way for the operational implementation of next-generation airborne SAR sensors, that will support the technological development of future spaceborne SAR missions, boosted by the increasing demand of earth surface monitoring of dynamic environmental processes.

REFERENCES

[1] A. Moreira, P. Prats-Iraola, M. Younis, G. Krieger, I. Hajnsek, and K. P. Papathanassiou, "A tutorial on synthetic aperture radar," *IEEE Geosci. Remote Sens. Mag.*, vol. 1, no. 1, pp. 6–43, Mar. 2013.

[2] M. Martone, P. Rizzoli, C. Wecklich, C. González, J.-L. Bueso-Bello, P. Valdo, D. Schulze, M. Zink, G. Krieger, and A. Moreira, "The global forest/non-forest map from TanDEM-X interferometric SAR data," *Remote Sens. Environ.*, vol. 205, pp. 352–373, Feb. 2018.

[3] S. Huber, F. Q. de Almeida, M. Villano, M. Younis, G. Krieger, and A. Moreira, "Tandem-L: A technical perspective on future spaceborne SAR sensors for earth observation," *IEEE Trans. Geosci. Remote Sens.*, vol. 56, no. 8, pp. 4792–4807, Aug. 2018.

[4] G. Krieger, M. Younis, S. Huber, F. Bordoni, A. Patyuchenko, J. Kim, P. Laskowski, M. Villano, T. Rommel, P. Lopez-Dekker, and A. Moreira, "Digital beamforming and MIMO SAR: Review and new concepts," in *Proc. 9th Eur. Conf. Synth. Aperture Radar*, Nuremberg, Germany, Apr. 2012, pp. 11–14.

[5] G. Krieger, M. Zonno, M. Rodriguez-Cassola, P. Lopez-Dekker, J. Mittermayer, M. Younis, S. Huber, M. Villano, F. Q. de Almeida, P. Prats-Iraola, and A. Moreira, "MirrorSAR: A fractionated space radar for bistatic, multistatic and high-resolution wide-swath SAR imaging," in *Proc. IEEE Int. Geosci. Remote Sens. Symp. (IGARSS)*, Fort Worth, TX, USA, Jul. 2017, pp. 149–152.

[6] R. Rincon, T. Fatoyinbo, B. Osmanoglu, S. K. Lee, C. F. D. Toit, M. Perrine, K. J. Ranson, G. Sun, M. Deshpande, J. Beck, D. Lu, and T. Bollian, "Digital beamforming synthetic aperture radar developments at NASA/Goddard space flight center," in *Proc. IEEE Int. Symp. Phased Array Syst. Technol. (PAST)*, Waltham, MA, USA, Oct. 2016, pp. 1–6.

[7] R. Horn, M. Jaeger, M. Keller, M. Limbach, A. Nottensteiner, M. Pardini, A. Reigber, and R. Scheiber, "F-SAR–recent upgrades and campaign activities," in *Proc. 18th Int. Radar Symp.* Prague, Czech Republic, Jun. 2017, pp. 1–10.

[8] Y. Zhou, W. Wang, Z. Chen, P. Wang, H. Zhang, J. Qiu, Q. Zhao, Y. Deng, Z. Zhang, W. Yu, and R. Wang, "Digital beamforming synthetic aperture radar (DBSAR): Experiments and performance analysis in support of 16-channel airborne X-band SAR data," *IEEE Trans. Geosci. Remote Sens.*, vol. 59, no. 8, pp. 6784–6798, Aug. 2021.

[9] A. Reigber, E. Schreiber, K. Trappschuh, S. Pasch, G. Müller, D. Kirchner, D. Geßwein, S. Schewe, A. Nottensteiner, M. Limbach, A. Schreiber, T. Rommel, R. Horn, M. Jäger, R. Scheiber, S. V. Baumgartner, S. K. Joshi, A. B. C. da Silva, and A. Moreira, "The high-resolution digital-beamforming airborne SAR system DBFSAR," *Remote Sens.*, vol. 12, no. 11, p. 1710, May 2020.

[10] R. F. Rincon, T. Fatoyinbo, K. J. Ranson, B. Osmanoglu, G. Sun, M. Deshpande, M. Perrine, C. D. Toit, Q. Bonds, J. Beck, and D. Lu, "The ecosystems SAR (EcoSAR) an airborne P-band polarimetric InSAR for the measurement of vegetation structure, biomass and permafrost," in *Proc. IEEE Radar Conf.*, Cincinnati, OH, USA, May 2014, pp. 1443–1445.

[11] P. Dubois-Fernandez, H. Cantalloube, B. Vaizan, G. Krieger, R. Horn, M. Wendler, and V. Giroux, "ONERA-DLR bistatic SAR campaign: Planning, data acquisition, and first analysis of bistatic scattering behaviour of natural and urban targets," *IEE Proc.-Radar, Sonar Navigat.*, vol. 153, no. 3, p. 214, 2006.

[12] A. Meta, C. Trampuz, A. Coccia, S. Placidi, L. C. I. Hendriks, M. Davidson, and D. Schuettemeyer, "Bistatic airborne SAR acquisitions at L-band by MetaSensing: First results," in *Proc. 12th Eur. Conf. Synth. Aperture Radar*, Aachen, Germany, Jun. 2018, pp. 1–5.

[13] V. W. Yohandri, I. Firmansyah, P. R. Akbar, J. T. S. Sumantyo, and H. Kuze, "Development of circularly polarized array antenna for synthetic aperture radar sensor installed on UAV," *Prog. Electromagn. Res.*, vol. 19, pp. 119–133, 2021.

[14] D. K. Sharma, B. K. Pandey, S. Kulshrestha, S. B. Chakrabarty, and R. Jyoti, "Design of wideband microstrip antenna array at L-band for synthetic aperture radar applications," *Microw. Opt. Technol. Lett.*, vol. 55, no. 4, pp. 903–908, Apr. 2013.

[15] T. Dong, K. Li, Z. Xia, and X. Li, "A low-profile shared-aperture dual-band broadband antenna array for SAR applications," in *Proc. 50th Eur. Microw. Conf. (EuMC)*, Utrecht, The Netherlands, Jan. 2021, pp. 37–40.

[16] Y. Chen and R. G. Vaughan, "Dual-polarized *L*-band and single-polarized *X*-band shared-aperture SAR array," *IEEE Trans. Antennas Propag.*, vol. 66, no. 7, pp. 3391–3400, Jul. 2018.

[17] L. L. Shafai, W. A. Chamma, M. Barakat, P. C. Strickland, and G. Seguin, "Dual-band dual-polarized perforated microstrip antennas for SAR applications," *IEEE Trans. Antennas Propag.*, vol. 48, no. 1, pp. 58–66, Jan. 2000.

[18] J. Li, J. Chen, W. Liu, P. Wang, and C. Li, "A synthetic bandwidth method for high-resolution SAR based on PGA in the range dimension," *Sensors*, vol. 15, no. 7, pp. 15339–15362, Jun. 2015.

[19] Y. Huang, Q. Zhang, and L. Ferro-Famil, "Forest height estimation using a single-pass airborne L-band polarimetric and interferometric SAR system and tomographic techniques," *Remote Sens.*, vol. 13, no. 3, p. 487, Jan. 2021.

[20] T. Kraus, M. Bachmann, L. Heiderich, G. Krieger, and A. Moreira, "Multistatic SAR imaging: Comparison of simulation results and experimental data," in *Proc. Int. Conf. Radar Syst.*, Oct. 2017, pp. 1–5.

[21] M. Coulombe, S. Farzaneh Koodiani, and C. Caloz, "Compact elongated mushroom (EM)-EBG structure for enhancement of patch antenna array performances," *IEEE Trans. Antennas Propag.*, vol. 58, no. 4, pp. 1076–1086, Apr. 2010.

[22] B. Mohamadzade and M. Afsahi, "Mutual coupling reduction and gain enhancement in patch array antenna using a planar compact electromagnetic bandgap structure," *IET Microw., Antennas Propag.*, vol. 11, no. 12, pp. 1719–1725, Sep. 2017.

[23] M. K. Khandelwal, B. K. Kanaujia, and S. Kumar, "Defected ground structure: Fundamentals, analysis, and applications in modern wireless trends," *Int. J. Antennas Propag.*, vol. 2017, pp. 1–22, Jan. 2017.

[24] M. Limbach, B. Gabler, R. Horn, A. Kosc, and A. Di Maria, "New cavity backed capacitively coupled stacked patch element for P-band SAR application," in *Proc. 8th Eur. Conf. Antennas Propag. (EuCAP)*, Apr. 2014, pp. 2030–2033.

[25] D. Lorente, M. Limbach, B. Gabler, H. Esteban, and V. E. Boria, "Sequential 90° rotation of dual-polarized antenna elements in linear phased arrays with improved cross-polarization level for airborne synthetic aperture radar applications," *Remote Sens.*, vol. 13, no. 8, p. 1430, Apr. 2021.

[26] D. Lorente, M. Limbach, B. Gabler, H. Esteban, and V. E. Boria, "Dual-polarized multilayer L-band asymmetric subarray with truncated electric walls separation for airborne SAR applications," in *Proc. 18th Eur. Radar Conf. (EuRAD)*, Apr. 2022, pp. 133–136.

[27] *Ansys HFSS*. Accessed: Oct. 30, 2023. [Online]. Available: https://www.ansys.com/en-gb/products/electronics/ansys-hfss/

[28] W. S. T. Rowe and R. B. Waterhouse, "Investigation into the performance of proximity coupled stacked patches," *IEEE Trans. Antennas Propag.*, vol. 54, no. 6, pp. 1693–1698, Jun. 2006.

[29] M. Bugaj and M. Wnuk, "Bandwidth optimization of aperture-coupled stacked patch antenna," in *Advancement in Microstrip Antennas with Recent Applications*. Rijeka, Croatia: InTechOpen, 2013.

[30] D. M. Pozar and S. D. Targonski, "Improved coupling for aperture coupled microstrip antennas," *Electron. Lett.*, vol. 27, no. 13, p. 1129, 1991.

[31] *High-Performance, Thin-Film Embedded Resistor Copper Foil*. Accessed: Oct. 4, 2023. [Online]. Available: https://ticertechnologies.com/

[32] *SMP*. Accessed: Oct. 5, 2023. [Online]. Available: https://www.rosenberger.com/product/smp/

[33] D. M. Pozar, "A review of aperture coupled microstrip antennas: History, operation, development and applications," Dept. Elect. Comput. Eng., Univ. Massachusetts Amherst, Amherst, MA, USA, Tech. Rep., May 1996. [Online]. Available: http://www.ecs.umass.edu/ece/pozar/aperture.pdf

[34] M. Limbach, B. Gabler, A. Di Maria, R. Horn, and A. Reigber, "DLR compact test range facility," in *Proc. 6th Eur. Conf. Antennas Propag. (EUCAP)*, Prage, Czech Republic, Mar. 2012, pp. 1276–1280.

DIEGO LORENTE received the degree in telecommunications engineering from Universitat Politècnica de València (UPV), Spain, in 2011. He is currently pursuing the Ph.D. degree with the German Aerospace Center (DLR), Oberpfaffenhofen, Germany. He is also a Research Scientist with the Microwaves and Radar Institute, DLR. His research interests include the design of low profile airborne radar antennas, the analysis of novel feeding topologies and highly integrated microwave structures, and the investigation of methods and techniques to deal with and suppress the external interactions of the antenna with its environment.

MARKUS LIMBACH is currently a Senior Research Associate and the Head of the Antenna Group, Microwaves and Radar Institute, German Aerospace Center (DLR), Oberpfaffenhofen, Germany. His research interests include antenna design and simulation for airborne synthetic aperture radar applications.

BERND GABLER (Member, IEEE) received the degree in telecommunications engineering from the Munich University of Applied Sciences, Germany, in 1990. He is currently a Senior Research Associate and the Head of the Compact Antenna Test Range of the Microwaves and Radar Institute, German Aerospace Center (DLR), Oberpfaffenhofen, Germany. His research interests include antenna and radar cross-section measurement techniques and analysis.

HÉCTOR ESTEBAN (Senior Member, IEEE) received the degree in telecommunications engineering from Universitat Politècnica de València (UPV), Spain, in 1996, and the Ph.D. degree, in 2002. He has collaborated with the Joint Research Center, European Commission, Ispra, Italy. He was with the European Topic Center on Soil (European Environment Agency), in 1997. He joined UPV, in 1998. His research interests include methods for the full-wave analysis of open-space and guided multiple scattering problems, the CAD design of microwave devices, the electromagnetic characterization of dielectric and magnetic bodies, the acceleration of electromagnetic analysis methods using the wavelets and the FMM, and the design and implementation of communication devices in substrate integrated technologies.

VICENTE E. BORIA (Fellow, IEEE) was born in Valencia, Spain, in 1970. He received the degree (Hons.) in ingeniero de telecomunicación and the Doctor Ingeniero de Telecomunicación degree from Universidad Politécnica de Valencia, Valencia, in 1993 and 1997, respectively. In 1993, he joined Departamento de Comunicaciones, Universidad Politécnica de Valencia, where he has been a Full Professor, since 2003. In 1995 and 1996, he held a Spanish Trainee position with the European Space Research and Technology Centre, European Space Agency, Noordwijk, The Netherlands, where he was involved in the area of electromagnetic analysis and design of passive waveguide devices. He has authored or coauthored 15 chapters in technical textbooks, 200 articles in refereed international technical journals, and over 250 papers in international conference proceedings. His current research interests include the analysis and automated design of passive components, left-handed and periodic structures, and on the simulation and measurement of high power effects in passive waveguide systems.